Soil temperature gradient as a useful tool for small water leakage detection from district heating pipes in buried channels

Matjaž Perpar*, Zlatko Rek

Laboratory for Fluid Dynamics and Thermodynamics, Faculty of Mechanical Engineering, University of Ljubljana, 1000 Ljubljana, Slovenia

*Corresponding author. Matjaž Perpar, Faculty of Mechanical Engineering, University of Ljubljana, Aškerčeva 6, 1000 Ljubljana, Slovenia, e-mail: matjaz.perpar@fs.uni-lj.si, Phone: +386 1 47 71 419, Fax: +386 1 47 71 447

Abstract

A methodology for detecting small leakages from pipelines placed in buried concrete channels is presented. This methodology is based on determining soil temperature gradient using appropriate numerical and experimental processes. An equivalent thermal conductivity (λ_{eq}) was defined based on the known heat flux and temperature gradient through the insulation subjected to the leakage. Two dimensional (2D) transient–steady-state–combined simulations were conducted for evaluating the channel cross-section heat loss. To mimic the leakage, λ_{eq} values in the range 0.5–10 W/(m·K) were used. The computation exhibited a large increase in the soil temperature gradient above the channel in case of leakage, from approximately 25 °C/m for dry insulation to approximately 50 °C/m at $\lambda_{eq} = 0.5$ W/(m·K). The procedure including the evaluation of the soil thermal conductivity λ_s, developed in our previous work, and further soil temperature gradient monitoring through computation and measurements enabled the detection of minor leakages in a pipeline section. Applying the proposed methodology to an entire network could contribute to comprehensive leakage control in district heating systems.

Highlights

- Insulation equivalent thermal conductivity (λ_{eq}) during the leakage was assessed
- 2D transient–steady-state–combined numerical simulations of heat loss were done
- Radiation within the channel was found to significantly contribute to heat loss
- Soil temperature gradient above the pipeline channel is a good leakage indicator

KEY WORDS: district heating, heat loss, numerical simulation, equivalent thermal conductivity, soil temperature gradient, leakage detection

1. Introduction

In this study, the possibility of detecting small water leakages in district heating (DH) systems was evaluated. The research refers to Ljubljana DH system where approximately 130 km of pipelines are placed in buried concrete channels. A majority of these pipelines were built more than 50 years ago. The total heat loss in the network (pipeline in channels and pre-insulated

pipeline) for the period 2005–2009 was 16.1% of the total heat input [1], which is similar to what was found elsewhere, for example 12–14% in Riga, Latvia [2] or 14.5% in Tallinn, Estonia [3]. In this study, 8.6% of the simulated total heat loss was observed during normal operation (dry insulation). Heat loss due to water runoff was estimated to be 1.5%. The remaining 6% loss corresponded mostly to the pipelines in the channels where the insulation damage or degradation appeared mainly because of leakage. Irrespective of the high cost, the systematic replacement of old pipelines in channels with the pre-insulated ones makes long term sense. In the last decade, renovation of 3–4 km of pipelines in the channels per year, supported by several leakage detection methods (aero thermography, manual IR camera, pressure tests, geophone, and monitoring the water amount added into the network) [4], helped the DH company in reducing total heat loss to approximately 12%. The smallest leakage was 2–3 m^3/h, which was detected by measuring the water level change in a heat storage tank connected to a selected closed area of the network.

DH companies generally control the network behavior by comparing simulated data at normal conditions with operational data. Apart from a sudden change in monitored data (pressure, flow rate, temperature), a long term discrepancy between simulated and measured data can indicate leakage. If the system is upgraded with detection equipment, e.g. resistance/impedance probes in pre-insulated pipes, the leak locations can be detected fairly accurately using suitable data analysis techniques. Such a data-driven method, which is based on correlating regularly monitored data with leakage data, is strongly affected by data quality [5]. Since small leakages cause small changes in the monitored parameters, detecting leakages below 2 m^3/h is extremely difficult, as illustrated by some examples of leak detection methods used so far. By utilizing the pressure wave-based method [6], a 10 t/h leak can be reliably detected, but a 1 t/h leak would be practically undetectable because of a significantly small pressure wave amplitude. Our experience [7] from the pressure drop measurements was similar: for a leak below 4 m^3/h, it was impossible to distinguish between the leak induced pressure drop and pressure fluctuations during normal operation. In another study [8], water loss was detected on the basis of the supply vs. return mass flow rate measurements utilizing roadside cabinets. The example demonstrated the possibility of measuring mass flow rate differences in the 5 m^3/h range. The leak detection method based on wide-band ground penetrating radar wave [9] is promising since it was successfully performed for water leakage occurring at 2 m^3/h.

One of the orientations towards the realization of the 4th generation DH concept is the transition to low supply and return temperatures [10]. The leakage in the network should be minimized to also reduce the heat demand. Although the thermography has a wide application potential [5], the method can be less accurate at lower DH network temperatures, especially for small leakages. Additionally, the exact temperature profile depends on several parameters and assumptions, e.g. the soil thermal conductivity and humidity, the structure of ground volume around the pipe, and surface conditions such as air temperature, surface cover, and wind [11].

Analysis of heat loss for DH network in Ljubljana was the background of this research. The previous study related to pre-insulated buried pipelines [12] was followed by this present study, which refers to pipelines in buried concrete channels. The analysis was aimed at finding the

method for detection of small leakages based on the fact that wet insulation contributes significantly more to the heat loss compared to dry insulation. A detection is necessary to locate the pipeline sections that must have a priority in the DH network reconstruction.

Heat transfer from a leaking pipe in the channel was analyzed numerically [13] via three regions: pipe insulation, channel cross-section and soil. The equivalent thermal conductivity (λ_{eq}) [14,15] of pipe insulation was obtained from the known heat flux and temperature gradient. Simulated as well as experimental results showed that λ_{eq} values in wet insulation can increase up to 25 W/(m·K). For the channel cross-section and soil, generally a steady-state calculation based on the heat transfer resistances of domain constituents is carried out [16–18]. In this study, 2D transient–steady-state–combined simulation (TSC) was used as a novel numerical procedure for resolving the air temperature stability. To mimic the leakage, the insulation λ_{eq} in the range 0.5 W/(m·K) to 10 W/(m·K) were used. Simulations showed a large increase of soil temperature gradient above the channel: from approximately 25 °C/m for dry to approximately 50 °C/m for wet insulation at $\lambda_{eq} = 0.5$ W/(m·K).

The key contribution of our study was using the soil temperature gradient as a potential leakage indicator. A procedure for successful small leak detection was proposed due to the doubling in the gradient magnitude. The methodology is useful especially for DH networks and can serve as a supplementary method to infrared thermography.

2. Numerical model

2.1. Pipe leakage

To the best of our knowledge, heat transfer in a two-phase flow inside the insulation of a DH pipeline was considered for the first time in this study. 3D transient simulations of the heat transfer through the insulation (porous media) were conducted for water leakage at a selected position on the pipe. The volume of fluid (VOF) model was adopted to capture the gas–liquid interface. The continuum surface force (CSF) model was applied for incorporating the surface tension effect. The Reynolds number, defined on the glass fiber of 5 μm diameter and inlet velocity 1.4 m/s, was Re = 7. As this value is much smaller than 100, the flow was considered as laminar, as per a previous study [19].

Time dependent laminar flow of an incompressible and immiscible gas-liquid two-phase system with heat transfer can be described with the following conservation equations. Compared to the single-phase flow simulations, the VOF method accomplishes interface tracking by solving an additional continuity-like equation for the liquid volume fraction.

$$\frac{\partial \alpha}{\partial t} + \frac{\partial}{\partial x_i}\left(\alpha u_i\right) = 0 \tag{1}$$

where α = 0 for gas phase, α = 1 for liquid phase, and 0 < α < 1 for a computational cell containing phase interface. The above equation is valid when there is no mass source and no mass transfer between phases (no phase change). The momentum [20,21] and energy [22] equations were solved as shown below.

$$\frac{\partial}{\partial t}(\rho u_i) + \frac{\partial}{\partial x_j}(\rho u_i u_j) = -\frac{\partial p}{\partial x_j} + \frac{\partial \sigma_{ij}}{\partial x_j} + \rho g_i + \sigma \kappa \frac{\partial \alpha}{\partial x_i}$$

(2)

$$\frac{\partial}{\partial t}(\rho E) + \frac{\partial}{\partial x_i}(u_i(\rho E + p)) = \frac{\partial}{\partial x_i}\left(\lambda \frac{\partial T}{\partial x_i}\right), E = h_s - p/\rho + u_i u_i / 2$$

(3)

The phases shared velocity and pressure fields. Eq. (2) and (3) depend on volume fractions of phases through material properties. Mixture material properties were determined by the following equation.

$$X = (1-\alpha) X_g + \alpha X_l$$

(4)

where X is for ρ, λ, c_p or μ, and indices l and g represent liquid and gas phase, respectively.

Geometry and operation data for the simulations were taken from [23]. The average nominal diameter (DN) of pipes in the channels was calculated to be 200 mm [1]. Therefore, this pipe dimension was considered for leakage simulations.

The computational domain, shown in Fig. 1, was represented by ½ of a cylindrical steel pipe with $D = 200$ mm, $b = 5.9$ mm, and $L = 1500$ mm. The space between the pipe and the outer aluminum foil of a thickness 0.2 mm was filled with mineral wool with a thickness of 100 mm. The domain was discretized with 672,599 control volumes (hexahedral cells: minimum orthogonal quality 0.885, maximum orthogonal skew 0.115, and maximum aspect ratio 3.066).

Air and water were used as working fluids. The physical properties of materials are shown in Table 1. Surface tension coefficient is 0.072 N/m.

Table 1
Material properties for the pipe leaking case.

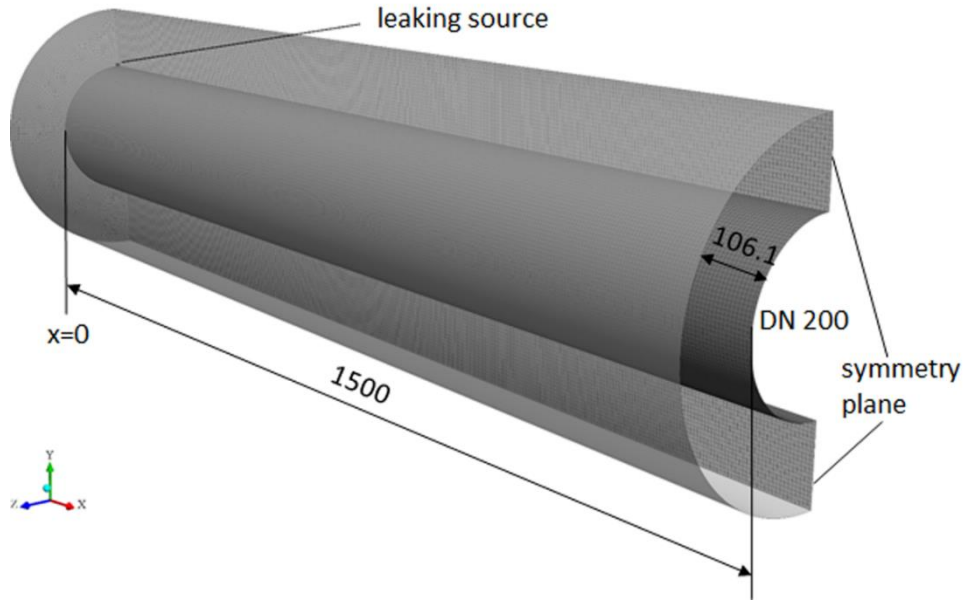| material	ρ, kg/m^3	c_p, J/(kg·K)	λ, W/(m·K)	μ, kg/(m·s)
water	998.2	4182	0.6	0.001
air	1.225	1006	0.024	1.789×10^{-5}
steel	8030	502.5	16.27	-
aluminum	2719	871	202.4	-
mineral wool	20	840	0.047	-

Fig. 1. Domain geometry and discretization for the pipe leaking case.

The fluid domain was treated as a porous zone. Two simulation cases were performed. For the first case, the insulation porosity of 0.974 and permeability factors, expressed here as viscous resistance coefficients $2.14592 \times 10^9 \, \mathrm{m}^{-2}$, $3.71747 \times 10^9 \, \mathrm{m}^{-2}$, and $2.7248 \times 10^9 \, \mathrm{m}^{-2}$ for axial, radial, and circumferential directions, respectively, were used [14]. For the second simulation case, the insulation porosity of 0.92 and viscous resistance coefficient of $2.7 \times 10^7 \, \mathrm{m}^{-2}$ were applied for all directions [24].

The boundary conditions were selected based on the experimental data [23,25]:
-   the leakage mass flow rate 0.03466 kg/s (Q = 500 l/h) or 0.0069 kg/s (Q = 100 l/h) with water temperature 76 °C has been prescribed at the leakage location ($x = 0$, $y = D/2$, $z = 0$),
-   leakage hole with 3 mm diameter,
-   gage pressure in the pipe as 5 bar,
-   outlet condition (zero gradient) in the y-z plane at $x = L$,
-   no-slip ($u_i = 0$) and $\theta_w = 76$ °C with shell conduction at the pipe internal wall ($r = D/2$),
-   no-slip and convection ($\theta_\infty = 27$ °C, h = 2.2 W/(m²·K) or 4.1 W/(m²·K)) with shell conduction at the aluminum foil external wall ($r = D/2 + b$),
-   symmetry in the y-z plane was at $x = 0$ and x-y plane was at $z = 0$.

A commercial computational fluid dynamics (CFD) code (ANSYS Fluent [13]) was used for the numerical simulation. An implicit pressure-based solver with the SIMPLE scheme for pressure-velocity coupling and bounded second order implicit transient formulation was used. The implicit scheme with a dispersed type of interface modelling was used for VOF. The least squares cell based spatial discretization was used for the gradient operator, whereas the pressure field was discretized with a PRESTO! scheme. For the momentum, energy, and volume fraction, the second order upwind discretization was used. The relaxation factors were set to 0.3 for pressure, 0.7 for momentum, and 0.5 for volume fraction. The fixed time step size Δt =

0.01 s was chosen such that the final time of 30 minutes was obtained in 180,000 steps. The convergence criteria condition within one time-step was 10^{-4} for all residuals or maximum 30 iterations, whichever was achieved earlier. One computation took between 16.6 and 68.2 days on 2 nodes (24 cores) of HPC cluster with Intel® Xeon® CPU X5670 @ 2.93 GHz processors.

2.2. Channel cross-section

A 2D TSC was used for evaluating heat transfer over the channel cross-section. Natural convection in the channel can be described with a continuity equation.

$$\frac{\partial \rho}{\partial t} + \frac{\partial}{\partial x_i}\left(\rho u_i\right) = 0 \tag{5}$$

together with momentum Eq. (2) (without the surface tension term) and energy Eq. (3). Due to the large temperature difference, the ideal gas law was used instead of the Boussinesq approximation for temperature dependent density [13]. The radiative heat transfer between solid surfaces is important. The ANSYS Fluent 17.2 has six radiation models available, but not all are appropriate for this case. This problem is very similar to our previous simulations [26], where the radiation models were compared with measured data. The Discreet Ordinate (DO) radiation model was found to be the most accurate and was thus used in this study. The radiative transfer equation is shown below.

$$\nabla \cdot \left(I\left(\vec{r},\vec{s}\right)\vec{s}\right) + (a+\sigma_s)I\left(\vec{r},\vec{s}\right) = an^2\frac{\sigma T^4}{\pi} + \frac{\sigma_s}{4\pi}\int\int_0^{4\pi}I\left(\vec{r},\vec{s}'\right)\Phi\left(\vec{s}\cdot\vec{s}'\right)d\Omega' \tag{6}$$

The computational domain is shown in Fig. 2a. The channel configuration for DN 200 was selected. The concrete channel was placed 0.9 m below the soil surface. The soil domain extended for 2 m to the left, right, and bottom of the channel. The supply and return pipes had 100 mm and 50 mm thick insulations, respectively.

The domain was discretized (Fig. 2b) with 93,793 control volumes (quadrilateral cells: minimum orthogonal quality 0.815, maximum ortho skew 0.185, and maximum aspect ratio 2.671). As in [12], a fine grid was used with 5 mm cell size for the insulation and 50 mm size for other domain regions.
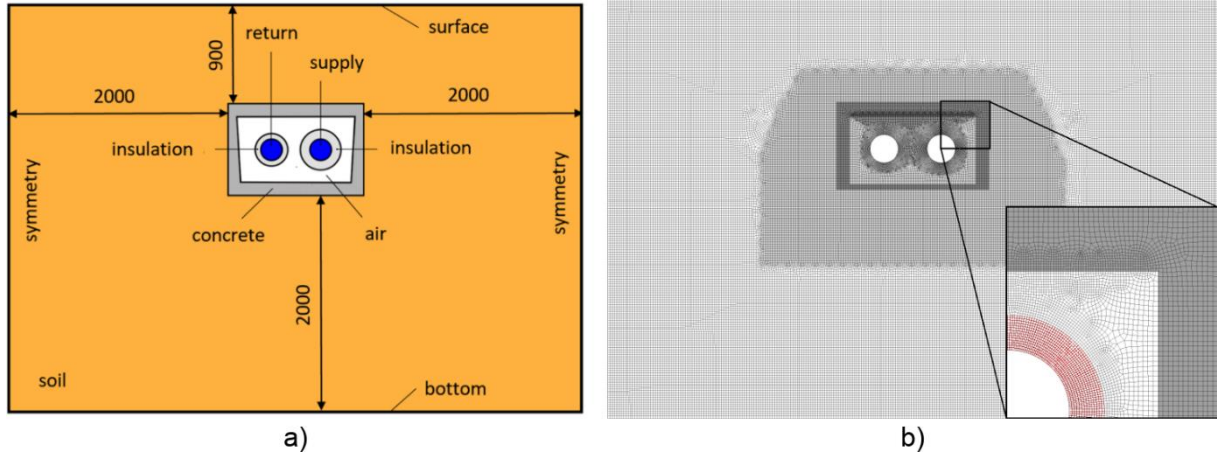
Fig. 2. a) Domain geometry of the channel cross-section and b) channel cross-section domain discretization.

Within the channel, between the insulation and concrete, air was used as the working fluid. The physical properties of the materials are summarized in Table 2. The insulation thermal conductivity values that are different from $\lambda = 0.047$ W/(m·K) are for the leakages (λ_{eq}). The insulation cover emissivity (ε) was selected as 0.93 and 0.07 for roofing cardboard and aluminum sheet, respectively.

The average of per day simulated heat loss for the year 2009 was equal to the heat loss of day 304, i.e. October 31 [1]. Therefore, boundary conditions referring to this day were used for the channel cross-section:
- temperature $\theta_{surf} = 3.7$ °C for soil surface (equal to the surrounding air temperature θ_a, sufficient condition due to low temperature difference [12]),
- temperature $\theta_s = 10$ °C at the bottom boundary (the undisturbed ground temperature),
- supply water temperature $\theta_{sup} = 100$ °C,
- return water temperature $\theta_{ret} = 60$ °C,
- symmetry at left and right boundaries,
- conjugate heat transfer trough soil, concrete, and insulation solid domains,
- radiative heat transfer between solid surfaces in contact with air,
- the air that is not participating in radiation transfer ($a = \sigma_s = 0$, n = 1).

Table 2
Material properties for the channel cross-section case.

material	ρ, kg/m³	c_p, J/(kg·K)	λ, W/(m·K)	μ, kg/(m·s)	ε, -
air	ideal gas	1006	0.024	1.789×10^{-5}	0
steel	8030	502.5	16.27	-	
concrete	2000	879	1.14	-	0.9
soil	1800	880	0.8	-	
insulation	20	840	0.047 to 10	-	0.93 or 0.07

The 2D solver was used for the numerical simulation. The Rayleigh number (Ra) was in the range of 5.9×10^5–1.4×10^6, indicating laminar flow [22]. A pressure-based solver with the SIMPLE scheme for pressure-velocity coupling was used. The first order implicit time formulation was applied in transient calculation. The Green-Gauss cell based spatial discretization was used for the gradient operator, whereas the pressure field was discretized with a PRESTO! scheme. For the density, momentum, and energy, the second order upwind discretization was used. The relaxation factors were set to 0.3 for pressure, 0.7 for momentum, and 1.0 for density and energy. The convergence criteria condition within one time-step was 10^{-12} for energy and 10^{-4} for all other residuals or a maximum of 20 iterations, whichever was achieved earlier.

The combined procedure was utilized to overcome the convergence problem arising due to different timescales. The heat diffusion timescale can be denoted as $\tau_{\mathrm{diff}} = L^2/a = 10^7$ s, where $L = 5$ m is characteristic length for the solid domain, and $a = \lambda/\rho c_p = 5 \times 10^{-7}$ m^2/s denoted soil thermal diffusivity. The corresponding material properties are summarized in Table 2. The convection timescale can be denoted as $\tau_{\mathrm{conv}} = L/U = 10$ s, where $L = 1$ m is the characteristic length for an air cavity and $U = 0.1$ m/s is the characteristic velocity for natural convection. Due to the different timescales the flow solution required a smaller time step, while the heat energy solution in solids (insulation, soil, concrete) generally takes a long time. The fulfilment of these conditions would require an excessive number of time steps. Hence, we used a TSC simulation. First, we conducted a transient computation with a fixed time step size ($\Delta t = 0.01$ s) and 6000 time steps to obtain an initial velocity field. Then, the momentum equation was turned off and only the energy equation was solved for the frozen velocity field. The procedure was repeated with $\Delta t = 0.1$ s and 3000 time steps and then repeated thrice with $\Delta t = 1$ s and 300 time steps. After 9900 time steps, the temperature at the sampled point, which was located midway between the supply and return pipe, was found to have converged. A steady-state computation was conducted after each time interval iteration. The last iteration, after the fifth iteration, represented the final simulation result. On the other hand, while using only steady-state simulation, the temperature did not converge after 10000 iterations, see Fig. 3. The temperature convergence history of the temperature refers to the channel geometric center.
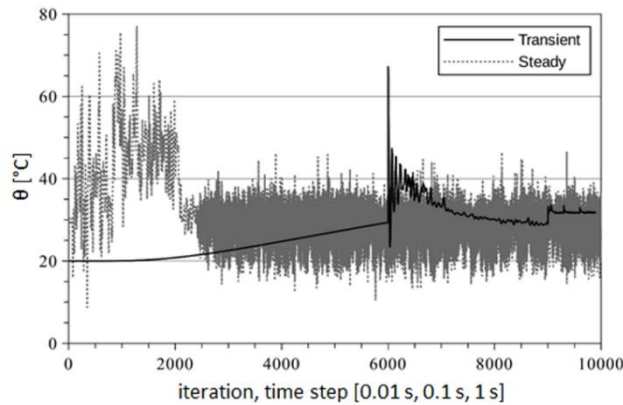

Fig. 3. Convergence history of the temperature in the midway point between the supply and return pipe.

3. Measurements

The schematic of the pipe leakage experiment is shown in Fig. 4a. A pilot test section was set up in the substation of the DH company as a bypass for the supply pipeline. The DN 200 pipe was insulated by 100 mm thick mineral wool covered with a 0.2 mm thick aluminum foil. To mimic leakage, a 3 mm inner diameter tube was embedded in the insulation atop the pipe. The water injection, provided from the supply, was oriented upwards in the middle of the 3 m long insulated section.

Outside insulation temperatures were measured at five longitudinal locations (x), where sensors (θ_{out}) were positioned in four main azimuths (0° for top, 90°, 180°, and 270°). To increase the reliability of surface temperature measurements, the sensors were fixed under the aluminum foil. The inside insulation temperature (θ_{in}) was obtained by measuring the outside wall temperature of the supply pipe, assumed to be equal along the pipe due to high steel thermal conductivity. Θ_a denotes the ambient air temperature. In-house constructed K-type thermocouples of 0.2 mm diameter were used. The leakage volume flow rate (500 l/h) was provided by pre-measuring the leaked water volume at a given time.
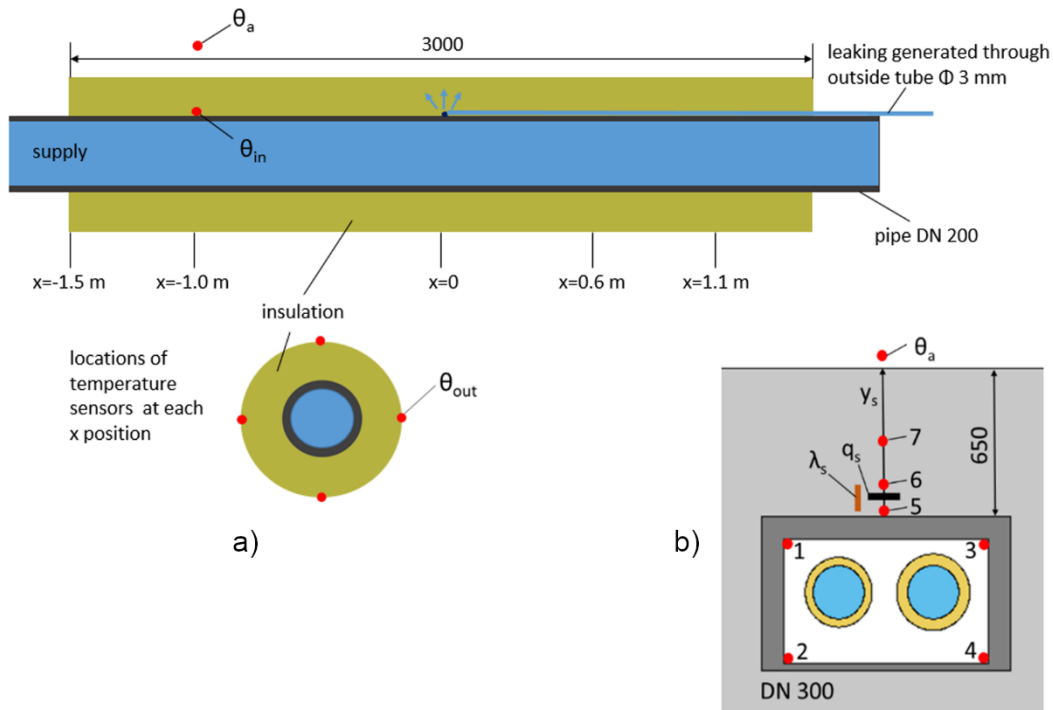

Fig. 4. Schematic of the experiments, a) is for the pipe leakage and b) is for the field measurements.

The schematic of the channel cross-section measurements is presented in Fig. 4b. The field measurements [1] were performed in the DN 300 channel. For the purpose of this research, the following experimental data was needed: temperatures in the channel inside the corners (positions 1 to 4), soil temperatures above the middle of the channel (positions 5 to 7),

temperature of the surrounding air (θ_a), heat flux density (q_s), and soil thermal conductivity (λ_s). Specifications and accuracy of the sensors are given in Table 3.

Table 3
Specifications and accuracy of the sensors.

Property	Manufacturer	Type	Range	Calibration	Accuracy
Temperature	Picotech	EL015	−30 to 70 °C	−11.5 to 60.3 °C	±0.5 °C
Temperature	Lascar	EL-USB-TC	−184 to 1373 °C	/	±1.0 °C
Soil therm. cond.	Hukseflux	TP01	0.3 to 4 W/(m·K)	/	±5%
Heat flux density	Hukseflux	HFP01	−2 to 2 kW/m^2	13.7 to 35.6 W/m^2	10 to 13%

4. Results and discussion

4.1. Equivalent thermal conductivity

Research on wet insulation properties is conducted in the domain of building construction. Different heat transfer mechanisms have already been considered for dry mineral wool [27]. The apparent thermal conductivity was estimated as the sum of four thermal conductivities: a) for the solid fibrous material, b) for the air in pores, c) due to effects of natural convection within the porous structure, d) due to thermal radiation between the fibers. Effective thermal conductivity was determined by including the morphological parameters of the mineral wool. On the other hand, the effective thermal conductivity for wet insulation [28,29] was defined as the sum of the constituents' conductivity and related volume fraction products. In [30], the thermal conductivity of wet hydrophilic mineral wool was measured in a wide range of the volume moisture content. The porous material's anisotropy was not found to be significant. Models for predicting mineral wool thermal conductivity, based on the constituents' volume fraction, were found to be unsatisfactory and sophisticated. Measurements showed that mineral wool thermal conductivity at saturation volumetric moisture content can be within 0.7 and 0.9 W/(m·K), depending on whether the mineral wool is hydrophobic or hydrophilic [31]. Both the mineral wool types were found to be highly permeable to water vapor.

In the DH domain, the insulation is exposed to higher temperatures, such as in building applications. This means that the influence of the processes associated with vapor pressure to heat transfer is greater as compared to other applications. The "real" insulation thermal conductivity must include, in addition to the conductivity of the constituents, the influence of the processes involved in the transport of liquid and vapor [14]. Computational tools were found useful to study the contribution of the abovementioned processes. In [28], a numerical experiment was performed using mineral wool with a water volume fraction of 0.73. Conduction, evaporation, and steam diffusion were considered. The insulation on the steel pipe was heated from hot water inside the pipe, and the surrounding air was used as a heat sink. The referred data [28] allowed us to calculate λ_{eq} as:

10

$$\lambda_{eq} = \frac{q_L \ln\left(\dfrac{D_{out}}{D_{in}}\right)}{2\pi\left(\theta_{in} - \theta_{out}\right)} \qquad (7)$$

where q_L is the heat loss linear density. D_{out} and D_{in} as well as θ_{out} and θ_{in} are for the outside and inside insulation diameter and temperature, respectively. The results showed that with higher water temperature, λ_{eq} increased due to condensation but decreased due to steam diffusion. λ_{eq} values as the result of conduction, evaporation, and steam diffusion contribution were 0.56, 0.75, and 1.00 W/(m·K) at water temperatures of 65, 90, and 110 °C, respectively. The expected λ_{eq} values owing to the evaporation (or presence) of water vapor and its diffusion [28] can supplement pipe leakage simulations where these effects were not included.

4.2. Pipe leakage

4.2.1. Simulation results

The numerical experiment was focused on the influence of the leaking water flow on heat loss. The transient simulations considering the three permeability factors were marked by "*Sim. 3p*" while the simulation considering one gas permeability factor, see section 2.1. was marked by "*Sim. 1p*". Fig. 5a shows the liquid volume fraction distribution after 15 min for both the insulation permeability cases at a leakage rate of $Q = 500$ l/h and heat transfer coefficient for surrounding air of $h = 2.2$ W/(m²·K). The permeability effect was evident. In the *Sim. 1p* case, the longitudinal distribution of the liquid phase was more uniform than in that in the *Sim. 3p* case. It can be seen from Fig. 5b that the temperature distribution was correlated to the liquid volume fraction distribution.
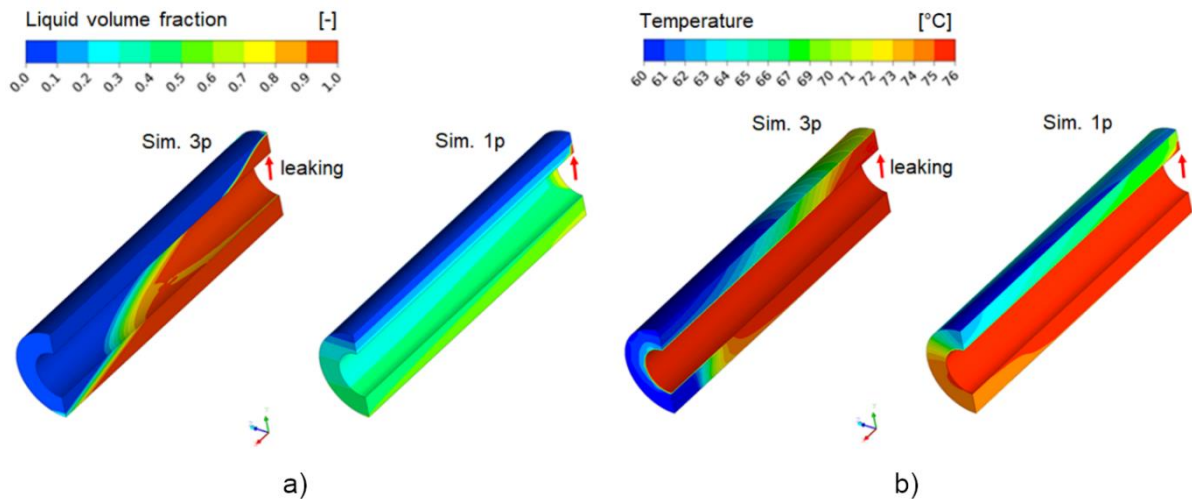

Fig. 5. a) Liquid volume fraction and b) temperature distribution after 15 min for both the insulation permeability cases, leakage rate at 500 l/h.

The temperature distribution results were used to calculate λ_{eq} by utilizing Eq. (7). The heat loss linear density (q_L) was obtained by

$$q_L = \pi h D_{out} \left(\theta_{out} - \theta_a \right) \tag{8}$$

with given air heat transfer coefficient h, air temperature θ_a, and insulation outside diameter D_{out}. θ_{out} and θ_{in} were taken as the arithmetic means of the outside and inside insulation temperatures, respectively, depicted with red points in the sketch A of Fig. 6. In this figure the dependence of λ_{eq} from x position at the simulation end time ($t = 0.5$ h) and air heat transfer coefficient ($h = 2.2$ W/(m²·K)) is shown.

In the *Sim. 3p* case, the highest λ_{eq} was 18.8 W/(m·K), obtained at the leakage injection location and with a leakage flow rate of 500 l/h. This value rapidly dropped below 4 W/(m·K) at the pipe section end. At the leakage flow rate of 100 l/h, the λ_{eq} values were significantly lower, from 2.75 W/(m·K) at the leakage inlet to approximately 1.5 W/(m·K) at other x positions. In the *Sim. 1p* case, λ_{eq} values were approximately 4 W/(m·K) and 1.5 W/(m·K) for leakage flow rates of 500 l/h and 100 l/h, respectively. These values were mostly independent of the x position. In conclusion, the differences in permeability have a major effect on λ_{eq} at the leakage site only.
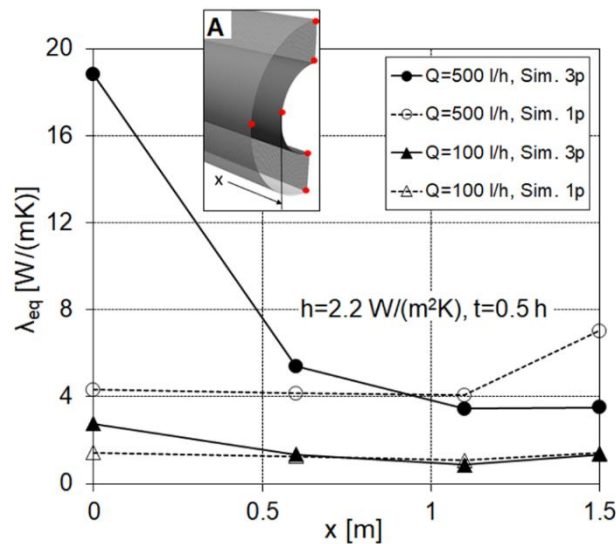

Fig. 6. Equivalent thermal conductivity as a function of the x position, the influence of the permeability factors. Sketch A shows the six positions where temperature data for the λ_{eq} calculations were taken.

The influence of different air heat transfer coefficients is presented in Fig. 7. The simulation results for *Sim. 3p* case exhibited practically no distinction in λ_{eq}.
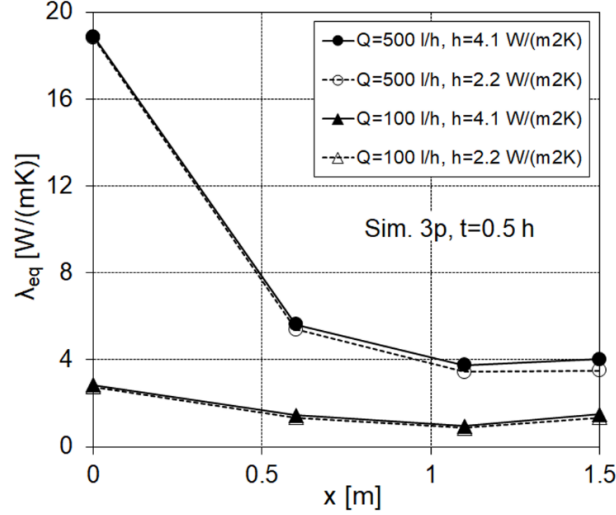
Fig. 7. Simulated equivalent thermal conductivity as the function of the *x* position, the influence of air heat transfer coefficient.

4.2.2. Experimental results

Experimental λ_{eq} values were calculated using Eq. (7), considering the arithmetic mean of the four outside insulation temperatures for θ_{out} and the supply pipe outside wall temperature for θ_{in}, see section 3. The air heat transfer coefficient *h* was calculated by the equation used for horizontal cylinders [22].

$$Nu_D = \left\{ 0.60 + \frac{0.387 Ra_D^{1/6}}{\left[1 + \left(0.559 / Pr \right)^{9/16} \right]^{8/27}} \right\}^2 \tag{9}$$

where Nu_D, Pr, and Ra_D stand for circumferential average Nusselt, Prandtl, and Rayleigh numbers, respectively. At Nu_D and Ra_D, the outside insulation diameter (D_{out}) was taken as the characteristic length. Ra_D was in the range of 10^7. The air heat transfer coefficient ($h = 4.1$ W/(m$^2 \cdot$K)) was determined as the average value for 26.6 h leakage measurements with a 1 min step, starting 1 h after the leakage inception. Because the insulation was covered by an aluminum foil, the radiation could be disregarded.

A time dependence of experimental equivalent thermal conductivity at the leakage inlet is shown in Fig. 8. Here, a small difference in q_L caused a significant increase in λ_{eq} as the outside insulation temperature increased. The dominant resistance to heat transfer was observed on the convection side. As shown in graph A of Fig. 8, the difference between the insulation outside and inside temperatures, denoted by "$x = 0$" and "pipe wall", respectively, decreased. As a consequence, λ_{eq} stabilized near 7 W/(m·K) 2 h after the leakage start, and then increased to 25 W/(m·K). High fluctuations are not relevant as they can be attributed to ±1 °C measurement accuracy.
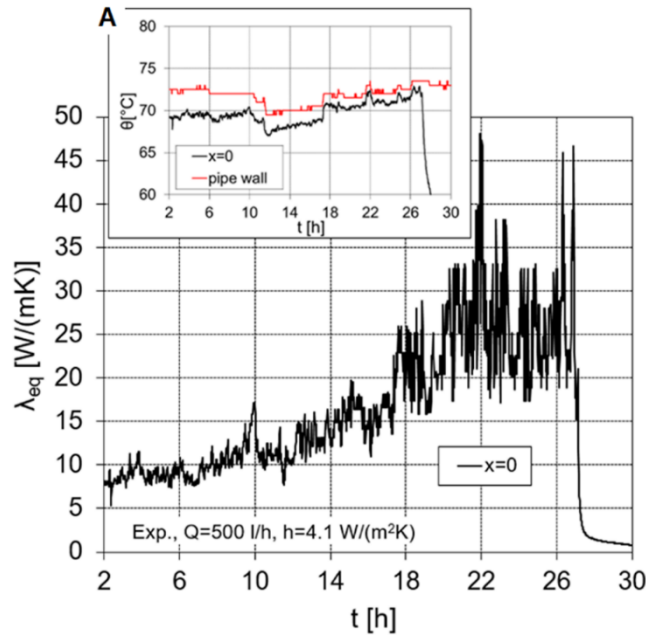
Fig. 8. Time dependence of experimental equivalent thermal conductivity at the leakage inlet. The graph A explains the increase and fluctuations of the thermal conductivity.

4.2.3. Comparison between the simulation and experiment

The experimental model could not match the simulation as:
- insulation was bent around a pipe. Deformation in radial direction changed the mineral wool density and consequently its porosity,
- the attachment by fastening clamps also deformed the wool structure.
- there was inhomogeneity within the wool,
- the contact between the pipe and wool was not tight. This gap was observed to be up to 10 mm. As a result, part of the leakage flow drained along the pipe.
- due to installation anomalies, the liquid flow induced heat transfer was reduced and probably replaced by the evaporation and vapor diffusion effects [28].

Because of the above-mentioned factors, the comparison between numerical and physical experiments can just be indicative.

The comparison of *Sim. 3p* simulations with the experiment for leakage rate $Q = 500$ l/h can be observed in Fig. 9. The results represent simulation end time of $t = 0.5$ h. The steady-state heat loss linear density as a function of λ_{eq} was obtained by determination of the overall heat transfer coefficient considering the heat conduction through the pipe wall, insulation (λ_{eq}), and aluminum foil together with the air heat transfer coefficient. The water side heat transfer coefficient was disregarded due to its insignificant contribution to the heat transfer resistance. The simulated and experimental λ_{eq} values, taken half an hour after the leakage started, were close to the steady-state values. Experimental data represent the averaged values within the time period of 26.6 h [25]. Experimental λ_{eq} for x positions away from the leakage inlet were between 0.8 and 1 W/(m·K). These values were much smaller compared to simulated ones but close to those obtained in [28], indicating the impact of evaporation and vapor diffusion in our

14

experiment. However, this was not the case for the leakage inlet where simulated and measured λ_{eq} values were much greater. Beside this, heat loss linear density was approximately 250 W/m for both the simulation and the experiment.
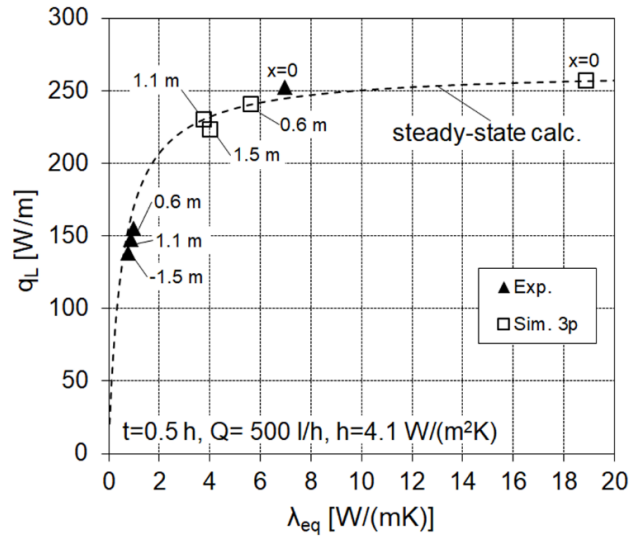

Fig. 9. Comparison of simulated and experimental heat loss linear density as a function of equivalent thermal conductivity.

4.3. Channel cross-section

4.3.1. Simulation results

According to the previous section, λ_{eq} values 0.5, 1, 5, and 10 W/(m·K) were selected to mimic different small leakage conditions. Based on the assumption that the leakage probability is the same for the supply and the return pipes, an equal λ_{eq} was chosen for both pipes. The contribution of radiation can be significant. Therefore, both the convection and radiation computation models were considered. Pipes are generally protected against outside water ingress by a roofing cardboard having high emission coefficient ($\varepsilon = 0.93$). To determine the contribution of radiation, simulations with convection model only were also performed. Fig. 10 presents the domain temperature fields for different λ_{eq} values and both the simulation cases. To mimic the leakage, $\lambda_{eq} = 0.5$ W/ (m·K) and $\lambda_{eq} = 1.0$ W/ (m·K) were used.
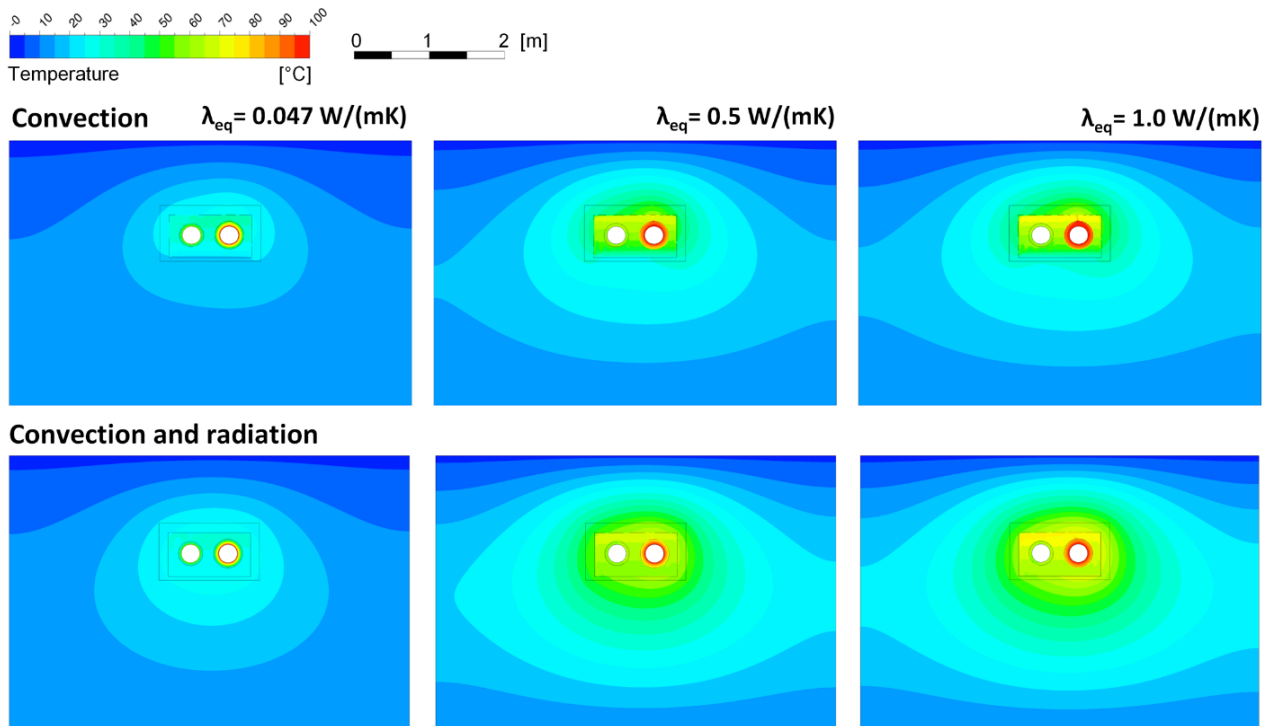
Fig. 10. Temperature fields of the channel domain for different λ_{eq} and two simulation cases within the channel: utilizing convection model or convection and radiation models.

Based on the analysis presented in section 4.2, it can be stated that the λ_{eq} values are quite probable for long term leakage. Significant soil temperature distribution change due to λ_{eq} increase was observed regardless of the selected computational model.

The temperature field of the channel cross-section for $\lambda_{eq} = 1.0$ W/(m·K) is shown in Fig. 11. In the convection model, the characteristic plume atop the supply pipe appeared. Air temperature field was more uniform when the radiation was included in the model.
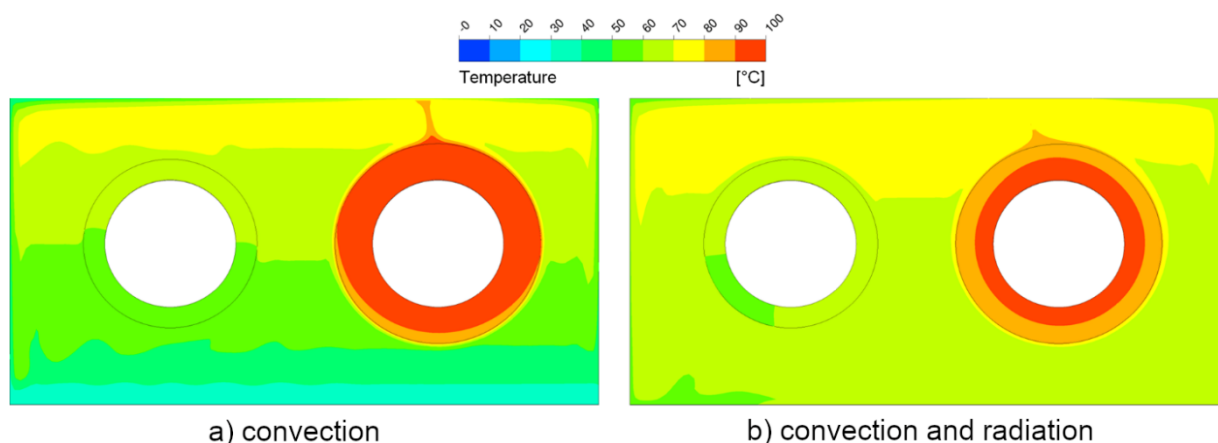

a) convection

b) convection and radiation

Fig. 11. Temperature field of the channel cross-section for $\lambda_{eq} = 1.0$ W/(m·K) for two simulation cases within the channel.

Streamline and velocity fields for both models are depicted in Fig. 12. Streamline regions A, B, and C appeared practically identical, as in the experiment performed in [32]. The authors reported a more or less triangular-shaped region A with eddy circulations around the cooler pipe. Next, a well-defined eddy (B) between the hotter pipe and the channel wall was observed. Finally, in the bottom part of the channel (region C), a weak and irregularly shaped swirl was observed. The main characteristic of the velocity field was higher velocities within the plume atop the supply pipe which caused the dominant air to move along the upper channel wall above the return pipe.
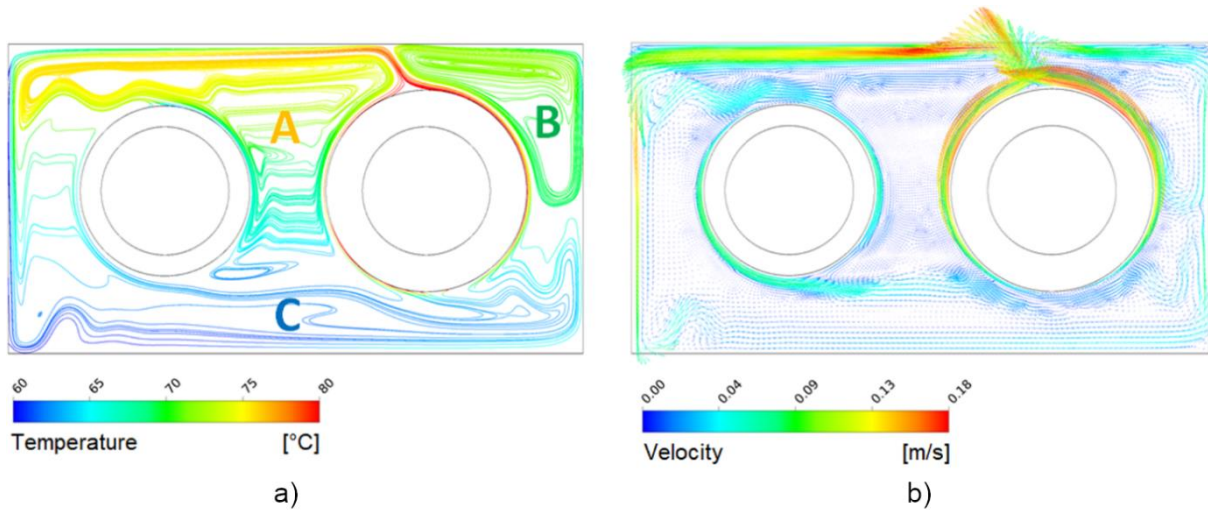

Fig. 12. Streamlines (a) and velocity field (b) of the air in the channel for the simulated case including convection and radiation models, $\lambda_{eq} = 1.0$ W/(m·K).

Heat loss linear density as a function of λ_{eq} for two simulation cases, separately for supply pipe, return pipe, and the sum of both is shown in Fig. 13a. Negative values for the return pipe are due to lower water temperature since the enlarged λ_{eq} caused a heat gain. The sum of both represented the channel. There was a sharp increase in heat loss from dry insulation, $\lambda_{eq} = 0.047$ W/(m·K), to $\lambda_{eq} = 0.5$ W/(m·K). At further increase in λ_{eq}, the increase the heat loss computed considering convection and radiation (*Con. & Rad.*) was significantly higher than the one computed by considering convection (*Con.*) only.

In Fig. 13b, both computational cases are presented via heat loss ratio (HLR), defined as the ratio between the heat loss linear density, computed for particular λ_{eq}, and its value for dry insulation. In the *Con.* Case, the heat loss increased by approximately 2.4 times while in the *Con. & Rad.* Case, it increased by approximately 3 times according to the dry insulation. By comparing *Con. & Rad.* vs. *Con.*, it was found that the radiation contributed to the heat loss with approximately 20% at dry insulation and up to 60% at higher λ_{eq}. It was also observed that if the insulation was wrapped by an aluminum sheet, the radiation contribution to the heat loss was approximately 5% for dry insulation and approximately 10% for insulation with $\lambda_{eq} = 1.0$ W/(m·K). The significant heat loss reduction by utilizing the low emissivity insulation cover is thus evident.
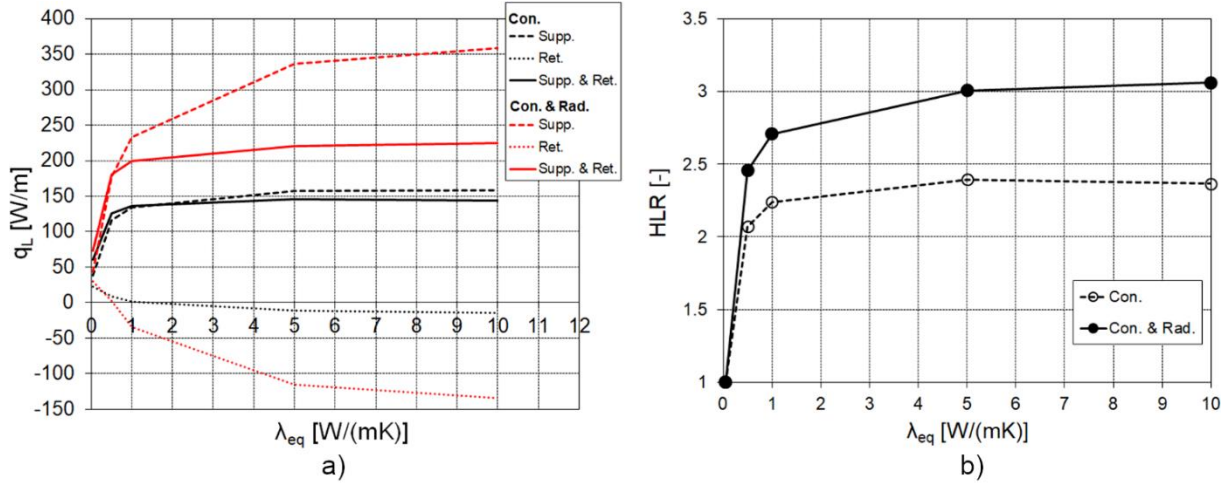
Fig. 13. a) Heat loss linear density and b) heat loss ratio as a function of λ_{eq}.

Our results simulated by the convection model are comparable with [29], where computed heat loss from two pipes in the channel was reported to be 2.08 times higher due to wet insulation (water volume fraction 0.73). This HLR value was almost similar to the value of 2.07 for $\lambda_{eq} = 0.5$ W/(m·K), obtained in this study. After [31], the measured insulation thermal conductivity of 0.5 W/(m·K) corresponded to the water volume fraction of approximately 0.75, which is similar to the value selected in [29]. When considering convection and radiation [33], the simulation for dry insulation showed that the radiation contributed an additional 16% to 18% heat loss, very close to the value of 21% obtained in this study.

The soil temperature profile was defined as the soil temperature dependence from the soil depth, measured in the direction y_s from the mid-point of the channel atop, see Fig. 4b. Fig. 14a shows the profiles obtained by considering the convection only. The lines represent linear regressions, where for all λ_{eq} choices, the R^2 value was greater than 0.99. The temperature profile slopes for $\lambda_{eq} = 0.5$ W/(m·K) and more were found to be much greater than for the dry insulation ($\lambda_{eq} = 0.047$ W/(m·K)), but not very different among themselves. At *Con. & Rad.* Computation, the linear regressions of soil temperature profiles were also characterized by $R^2 > 0.99$ for all λ_{eq}. The comparison of the profiles for *Con.* and *Con. & Rad.* computations for two selected λ_{eq} is presented in Fig. 14b. There was practically no slope difference for $\lambda_{eq} = 0.047$ W/(m·K), but the difference was significant for $\lambda_{eq} = 1.0$ W/(m·K).
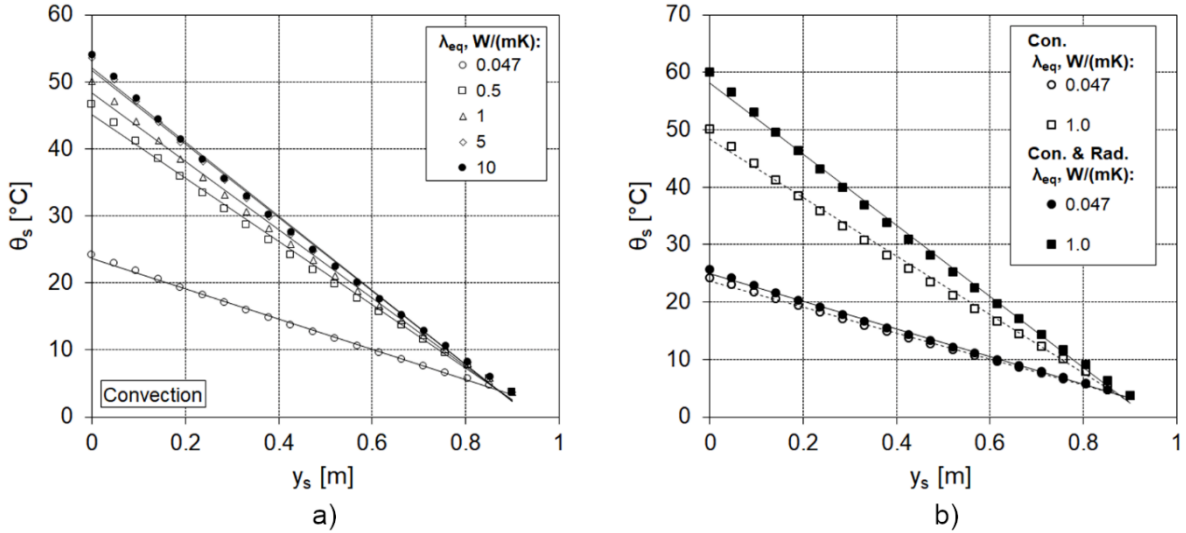
18

Fig. 14. Simulated soil temperature profiles above the channel for: a) various λ_{eq} values utilizing convection model, and b) two λ_{eq} values utilizing two computation cases.

4.3.2. Experimental results

Measured data for the case of dry insulation showed the influence of θ_a on the soil temperature gradient, see Fig. 15. The pipeline daily averaged heat load varied, as depicted by variations in q_s. The soil temperature gradients from 26.3 °C/m to 14.6 °C/m at air temperatures from 3.1 °C to 15.8 °C were much lower than those expected for the leakage event (over 50 °C/m).
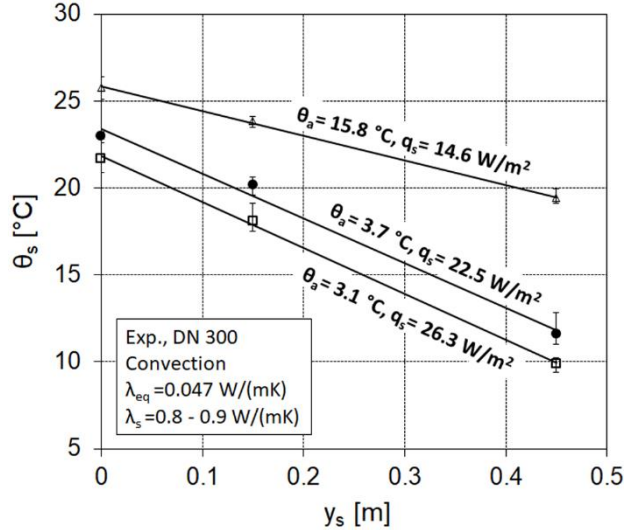

Fig. 15. Soil temperature profiles and heat flux densities for different surrounding air temperatures.

4.3.3. Comparison between the simulation and experiment

A comparison was performed for the convection case (the pipeline was covered with the aluminum sheet) at dry insulation, $\lambda_{ef} = 0.047$ W/(m·K). Two operational conditions were considered: for the reference day 304 and for day 284 with the same λ_s (0.8 W/(m·K)) but different surrounding air and supply temperatures, see Table 4. The temperature sensor

19

positions are depicted in Fig. 5b. The difference between simulated and experimental values was within −4.1 °C and +3.3 °C for day 304 and within −3.6 °C and +1.9 °C for day 284. These ranges agree well with 95% confidential limits of −3.2 °C and +4.1 °C, obtained by the comparison of simulated (transient) and measured soil temperatures for the period of 63 days, see [12]. Since the present valuation included solid/gas contact temperatures (positions 1 to 4), the simulation appears to be reliable, which is also supported by similarities between simulated and measured heat flux densities for both days.

Table 4
Comparison between the simulation and experimental data for different operation days: a) October 31, 2009 and b) October 11, 2009.

a) Day 304, $\theta_a = 3.7$ °C, $\theta_{sup} = 100$ °C, $\theta_{ret} = 60$ °C

Position	1	2	3	4	5	6	7	
Property				θ (°C)				q_s (W/m^2)
Simulation	22.4	20.3	25.4	20.7	21.4	17.6	9.1	21.9
Experiment	26.5	17.0	29.4	21.7	23.0	20.2	11.6	22.5
Sim. – Exp.	−4.1	3.3	−4.0	−1.0	−1.6	−2.6	−2.5	−0.6

b) Day 284, $\theta_a = 15.8$ °C, $\theta_{sup} = 81$ °C, $\theta_{ret} = 63$ °C

Position	1	2	3	4	5	6	7	
Property				θ (°C)				q_s (W/m^2)
Simulation	28.8	22.3	28.1	21.8	27.7	25.3	19.5	14.8
Experiment	27.4	23.2	30.4	25.4	25.8	23.8	19.4	14.6
Sim. – Exp.	1.4	−0.9	−2.3	−3.6	1.9	1.5	0.1	0.2

4.4. Methodology for leakage detection

Soil temperature gradients as a function of λ_{eq} were compared, as shown in Fig. 16. The slope of approximately 25 °C/m at $\lambda_{eq} = 0.047$ W/(m·K) increased to over 50 °C/m or 60 °C/m for *Con.* or *Con. & Rad.* computation ($\lambda_{eq} = 0.5$ W/(m·K) and more), respectively.
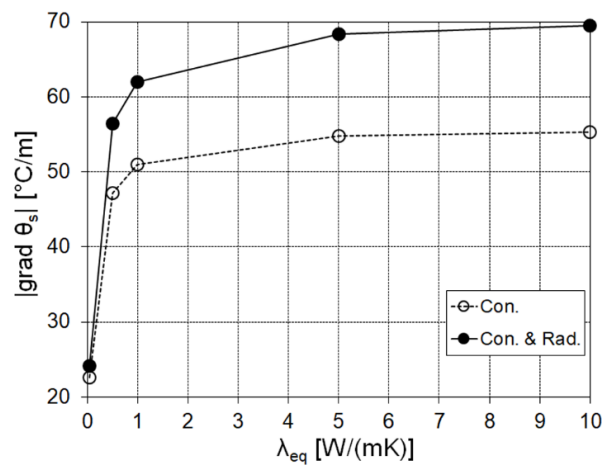

Fig. 16. Soil temperature gradient as a function of λ_{eq} for two computation cases.

There was similarity between the heat loss ratio (Fig. 13b) and soil temperature gradient (Fig. 16) as the function of λ_{eq}, as shown in Fig. 17. Here, a strong linear correlation between the heat loss ratio and the soil temperature gradient gives the opportunity to distinguish between normal and wet pipeline operation. Moreover, radiation was no longer relevant as both correlations (*Con.* or *Con. & Rad.*) had practically the same slope.
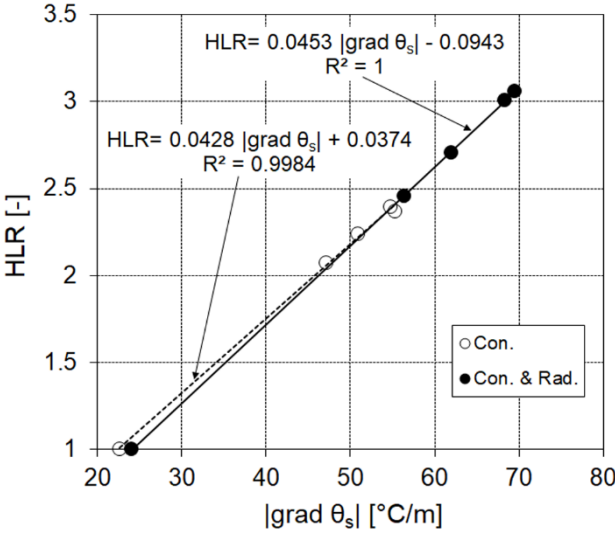

Fig. 17. Correlation between heat loss ratio and soil temperature gradient for two simulation cases.

The proposed leakage identification was based on the determination of soil temperature gradient. It is of crucial importance to ascertain the "base" gradient, which corresponds to a non-leakage operation. This is highly dependent on λ_s, as shown by simulated temperature profiles for λ_s between 0.4 W/(m·K) and 1.2 W/(m·K) in Fig. 18. The data corresponded to the DN 300 channel, see Fig. 4b. Only convection was considered since the pipeline insulation was covered with an aluminum sheet. For measured λ_s = 0.8 W/(m·K) on day 304, the simulated and measured temperatures were different, and this temperature shift was probably due to time dependent heat transfer history at the measured site. On the other hand, the temperature gradient was similar for the simulation and measurements. Additionally, the measured soil heat loss density (22.5 W/m²) was not very different from the computed value (21.9 W/m²).
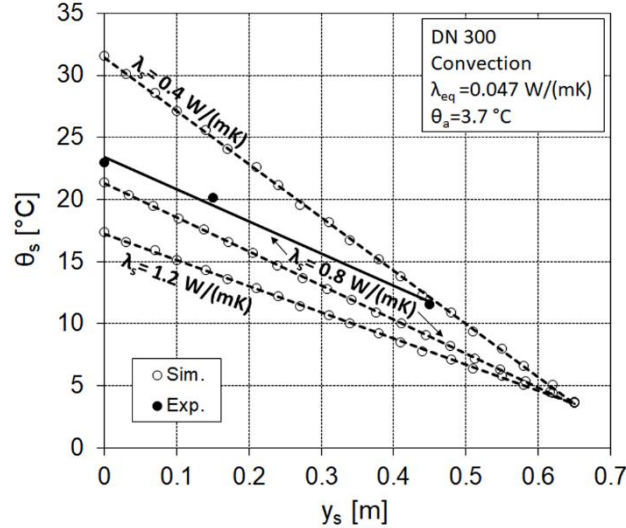
Fig. 18. Influence of various soil thermal conductivity values on the soil temperature profile.

For successful small leak detection in the DH channels, the following procedure is proposed:

1) Carrying out temperature measurements of supply, return, surrounding air, and soil above the channel.

2) Performing simulations for different values of λ_s.

3) Determining the actual λ_s based on the best match between simulated and measured soil temperatures, as presented in [12]. Additional check: matching of computed and measured soil temperature gradient.

4a) If λ_s is 0.8 W/(m·K) or more, i.e. at $\left| \text{grad } \theta_s \right|$ near 25 °C/m or less (see Fig. 18), the pipeline is considered under normal operation and no additional action is needed.

4b) If λ_s is small, e.g. 0.4 W/(m·K) or less, i.e. at $\left| \text{grad } \theta_s \right|$ near 40 °C/m or more (see Fig. 18), there are two possibilities:
   - the soil is very dry and the pipeline is in normal operation or
   - the pipeline is leaking.
Channel inspection is recommended.

5. Conclusions

The methodology for small leakage detection from district heating pipes in buried channels is presented. It is based on the soil temperature gradient determination that required appropriate numerical and experimental implementation. For the latter, only temperature sensors, relatively cheap and of high accuracy, are required. The 3D transient simulations of the heat transfer through the insulation (mineral wool) at small leakage flows were conducted using the ANSYS Fluent software and the VOF model (VOF). The λ_{eq}, obtained from the known heat flux and temperature gradient through the insulation, was used as the heat loss control parameter. The

results for the leakage inlet position, also consistent with the experiment, indicated large λ_{eq} values (up to 25 W/(m·K)).

2D TSC simulations were carried out as a novel method for evaluating the channel cross-section heat loss. The combined procedure was utilized to overcome the convergence problem due to different heat diffusion characteristic timescales. To mimic the leakage, λ_{eq} values within 0.5 W/(m·K) and 10 W/(m·K) were used. The computation showed a large increase in the soil temperature gradient above the channel in the leakage case: from approximately 25 °C/m for dry insulation to approximately 50 °C/m at $\lambda_{eq} = 0.5$ W/(m·K).

The proposed leakage detection procedure includes the evaluation of λ_s, as developed in [12], and further soil temperature gradient monitoring through computation and measurements. Both can lead to successful small leakage detection in the pipeline section. Applying the methodology for the whole network area could contribute to comprehensive leakage control in the DH system.

Acknowledgements

Nomenclature

a	absorption coefficient (-)
b	wall thickness (mm)
c_p	specific heat (J kg^{-1} K^{-1})
D	pipe diameter (mm)
g_i	gravity acceleration (m s^{-2})
h	heat transfer coefficient (W m^{-2} K^{-1})
h_s	sensible enthalpy (J kg^{-1})
I	radiation intensity (W sr^{-1})
L	pipe length (mm)
$\dot{m}$	mass flowrate (kg s^{-1})
n	refractive index (-)
Nu	Nusselt number (-)
p	pressure (N m^{-2})
Pr	Prandtl number (-)
q	heat flux density (W m^{-2})
q_L	heat flux linear density (W m^{-1})
Q	volume flowrate (l h^{-1})
r	pipe radius (mm)
$\vec{r}$	position vector (m)
Ra	Rayleigh number (-)
Re	Reynolds number (-)

$\vec{s}$	directional vector (m)
$\vec{s}\,'$	scattering direction vector (m)
T	absolute temperature (K)
t	time (s, hour)
u_i	velocity (m s^{-1})
x_i	Cartesian coordinate (m)

Greek symbols

α	liquid volume fraction (-)
Δ	delta/difference
ε	emissivity (-)
θ	temperature (°C)
κ	interface curvature (m^{-1})
λ	thermal conductivity (W m^{-1} K^{-1})
μ	dynamic viscosity (kg m^{-1} s^{-1})
ρ	density (kg m^{-3})
σ	surface tension coefficient (N m^{-1})
	Stefan-Boltzmann constant (W m^{-1} K^{-4})
σ_s	scattering coefficient (m^{-1})
σ_{ij}	stress tensor (N m^{-2})
Φ	phase function (-)

Subscripts

a	air
conv	convection
diff	diffusion
eq	equivalent
in	pipe inside wall
out	pipe outside wall
ret	return
s	soil
sup	supply
surf	surface
w	wall

Abbreviations

CFD	computational fluid dynamics
CSF	continuum interface force
DH	district heating
DN	nominal diameter
HLR	heat loss ratio
HPC	high performance computing
PRESTO!	PREssure STaggering Option (pressure interpolation scheme)
SIMPLE	Semi IMplicit Pressure Linked Equation
TSC	transient-steady-state-combined

VOF   volume of fluid

References

[1]   Žun I, Perpar M, Rek Z, Gregorc J. Setting up of heat loss physical model for DH system in Ljubljana. Report EN10-R7 (in Slovene). Ljubljana: 2010.

[2]   Ziemele J, Gravelsins A, Blumberga A, Blumberga D. Combining energy efficiency at source and at consumer to reach 4th generation district heating: Economic and system dynamics analysis. Energy 2017;137:595–606. doi:10.1016/j.energy.2017.04.123.

[3]   Volkova A, Mašatin V, Siirde A. Methodology for evaluating the transition process dynamics towards 4th generation district heating networks. Energy 2018;150:253–61. doi:10.1016/j.energy.2018.02.123.

[4]   Matičič P, Trunkelj S. Ensuring high reliability of Energetika Ljubljana district heating systems. Int. Conf. Dist. Energy, Portorose, Slovenia: 2017.

[5]   Zhou S, O'Neill Z, O'Neill C. A review of leakage detection methods for district heating networks. Appl Therm Eng 2018;137:567–74. doi:10.1016/j.applthermaleng.2018.04.010.

[6]   Valinčius M, Vaišnoras M, Kaliatka A. Study and demonstration of pressure wave-based leak detection in a district heating network. Struct Infrastruct Eng 2018;14:151–62. doi:10.1080/15732479.2017.1330892.

[7]   Perpar M, Gregorc J, Cotič M, Žun I. Identification of water leakage sources in the Ljubljana district heating system on the basis of pressure dynamics measurements and analysis within the closed areas. Report EN14-R16 (in Slovene). Ljubljana: 2014.

[8]   Filippini E, Marini I, Ongari M, Pedretti E. District heating leakage measurement: Development of methods. Energy Procedia 2018;149:297–306. doi:10.1016/j.egypro.2018.08.193.

[9]   Cheung BWY, Lai WWL. Field Validation of Water Pipe Leak by Spatial and Time-lapsed Measurement of GPR Wave Velocity. 2018 17th Int Conf Gr Penetrating Radar, GPR 2018 2018:1–4. doi:10.1109/ICGPR.2018.8441668.

[10]   Lund H, Werner S, Wiltshire R, Svendsen S, Thorsen JE, Hvelplund F, et al. 4th Generation District Heating (4GDH). Integrating smart thermal grids into future sustainable energy systems. Energy 2014;68:1–11. doi:10.1016/j.energy.2014.02.089.

[11]   Friman O, Follo P, Ahlberg J, Sjokvist S. Methods for large-scale monitoring of district heating systems using airborne thermography. IEEE Trans Geosci Remote Sens 2014;52:5175–82. doi:10.1109/TGRS.2013.2287238.

[12]   Perpar M, Rek Z, Bajric S, Zun I. Soil thermal conductivity prediction for district heating pre-insulated pipeline in operation. Energy 2012;44:197–210. doi:10.1016/j.energy.2012.06.037.

[13]   ANSYS®. Academic Research CFD, Release 17.2 n.d.

[14]   Marmoret L. Assessment of hydrothermal performance by thermophysical characterization of a crimped glass wool building insulation. J Build Phys 2017;40:401–16. doi:10.1177/1744259116649322.

[15]   Koči V, Maděra J, Jerman M, Trník A, Černý R. Determination of the equivalent thermal conductivity of complex material systems with large-scale heterogeneities. Int

J Therm Sci 2014;86:365–73. doi:10.1016/j.ijthermalsci.2014.07.020.

[16] Çomakli K, Yüksel B, Çomakli Ö. Evaluation of energy and exergy losses in district heating network. Appl Therm Eng 2004;24:1009–17. doi:10.1016/j.applthermaleng.2003.11.014.

[17] Hlebnikov A. The Analysis of Efficiency and Optimization of District Heating Networks in Estonia. Doctoral thesis 2010; Tallinn University of Technology, Faculty of Mechanical Engineering, Estonia. n.d.

[18] Sartor K, Quoilin S, Dewallef P. Simulation and optimization of a CHP biomass plant and district heating network. Appl Energy 2014;130:474–83. doi:10.1016/j.apenergy.2014.01.097.

[19] Jin Y, Kuznetsov A V. Turbulence modeling for flows in wall bounded porous media: An analysis based on direct numerical simulations. Phys Fluids 2017;29:045102. doi:10.1063/1.4979062.

[20] Faghri A, Zhang Y. Transport Phenomena in Multiphase Systems. 2006.

[21] Brackbil J, Kothe DB, Zemach C. A continuum method for modeling surface tension. J Comput Phys 1992;100:335–54. doi:10.1016/0021-9991(92)90240-Y.

[22] Incropera F, DeWitt D. Fundamentals of heat and mass transfer. 5th ed. New York: John Wiley & Sons; 2002.

[23] Perpar M, Lojevec N, Gregorc J, Zlatko R, Žun I. Setting up of heat loss physical model for DH system in Ljubljana. Report EN12-R15 (in Slovene). Ljubljana: 2013.

[24] www.ursa.si/assets/uploads/files/ursa-1491829125.pdf (in Slovene); August, 2019. n.d.

[25] Perpar M, Lojevec N, Gregorc J, Rek Z, Bajrić S, Žun I. Heat loss evaluation in wet insulation of district heating pipeline in Ljubljana. Int. Conf. Dist. Energy, Portorose, Slovenia: 2014.

[26] Rek Z, Rudolf M, Žun I. Application of CFD simulation in the development of a new generation heating oven. Strojniški Vestn - J Mech Eng 2012;58:134–44. doi:10.5545/sv-jme.2011.163.

[27] Humaish H, Marmoret L, Pelegris C, Beji H. Effect of "crimped" glass wool structure on effective thermal conductivity. High Temp - High Press 2017;46:3–22.

[28] Polovnikov VY, Gubina E V. Heat loss of heat pipelines in insulation moisture conditions with the evaporation. MATEC Web Conf 2014;19. doi:10.1051/matecconf/20141901008.

[29] Polovnikov VY. Numerical Investigation of the Thermal Regime of Underground Channel Heat Pipelines Under Flooding Conditions with the Use of a Conductive-Convective Heat Transfer Model. J Eng Phys Thermophys 2018;91:471–6. doi:10.1007/s10891-018-1766-3.

[30] Antepara I, Fiala L, Pavlík Z, Černý R. Moisture dependent thermal properties of hydrophilic mineral wool: Application of the effective media theory. Medziagotyra 2015;21:449–54. doi:10.5755/j01.ms.21.3.7334.

[31] Jerman M, Černý R. Effect of moisture content on heat and moisture transport and storage properties of thermal insulation materials. Energy Build 2012;53:39–46. doi:10.1016/j.enbuild.2012.07.002.

[32] Haq RFB, Probert SD, Shilston MJ. Steady state heat losses from horizontal pipes in

air-filled rectangular concrete duct. Proc Instn Mech Engrs 1985;199:203–13.

[33]   Kuznetsov GV, Polovnikov VY. Heat losses of underground channel heat pipes under conditions of deformation of the thermal insulation layer taking into account radiation heat transfer in the channel cavity. Eng Constr J 2012;28:2–7. doi:10.5862 / MCE.28.1.